MATERIALS CHEMISTRY FRONTIERS

RESEARCH ARTICLE

View Article Online
View Journal | View Issue

Cite this: *Mater. Chem. Front.*, 2021, **5**, 7241

Polymeric hole-transporting material with a flexible backbone for constructing thermally stable inverted perovskite solar cells†

Wenhua Zhang, Xueping Zong,* Ming Luo, Mengnan Hua, Lianjie Zhu, Mao Liang and Song Xue*

The explored p–i–n inverted architecture perovskite solar cells (i-PSCs) show promising application in flexible, large-scale and laminated photovoltaic technology. Polymeric HTMs for i-PSCs have been rarely reported. Thus far, only a commercial hole-transporting material, polytriarylamine (PTAA), has achieved a significant PCE of over 23% in i-PSCs. However, a perovskite precursor exhibits poor wettability on the PTAA films, thereby reducing their reproducibility and causing uncontrollable device instability. In this study, a type of binaphthyl-ether based polymer Z13 was developed through radical polymerization to replace the palladium catalyzed coupling reaction. A small molecule (Z5) and commercial PTAA were classified as the control. The comparatively flexible ether bond (–O–) of the backbone in Z13 improved the solubility and film forming properties of the material, thereby contributing to a superior morphology uniformity of the deposited perovskite. Consequently, promising device performance was achieved for i-PSCs endowed with Z13. The maximum power conversion efficiency of 18.80% obtained for Z13 was comparable with that of PTAA (19.02%), exceeding that with Z5 (18.48%). More importantly, Z13 films ensured a significantly optimized device thermal-durability as opposed to references PTAA and Z5. This study proposed a promising design for novel polymeric materials with low costs, high production reproducibility, favorable solubility and excellent optoelectronic properties.

Received 16th June 2021,
Accepted 16th August 2021

DOI: 10.1039/d1qm00869b

rsc.li/frontiers-materials

Introduction

Perovskite solar cells (PSCs) refer to a type of novel solar cell based on organic–inorganic halide perovskite materials. In 2009, when PSCs were initially introduced, their power conversion efficiency (PCE) was only 3.8%, whereas, 10 years later, the certified PCE reached up to 25.5%, and the PCE exhibited by perovskite-Si laminated photovoltaic devices was as high as 29%.[1–8] However, the poor stability of PSCs restricts their commercial applications. Accordingly, to sustainably develop energy and protect the environment, it is of great practical significance to optimize the vital materials of PSCs to ensure an efficient photoelectric conversion and prolong device stability simultaneously.[9,10]

Hole-transporting materials (HTMs) act as crucial components of highly efficient PSCs, and are indispensable in hole extraction, transport and suppression of charge recombination.[10–12] Researchers have developed a wide range of dopant-free organic HTMs, including small molecular compounds and polymers.[13–15] As compared with small molecular compounds, polymers exhibit better thermal stability, interfacial adhesion and film toughness. Over the past few years, the application of dopant-free polymer molecules in PSCs has aroused enormous attention *e.g.*, random copolymers (PTEG)[16] comprising benzo[1,2-*b*:4,5:*B*′]dithiophene (BDT) and 2,1,3-benzothiadiazole (BT), efficient polymeric (DTB(*x*DEG)[17] through side-chain engineering, and donor–acceptor type polymers (PBT1-C)[18] by copolymerizing (BDD) with the BDT backbone and a BDT derivative P3.[19] Recently, Li and Guo[20] devised a series of amino-modified BDT derivatives, in which the PBDT-N20 based PSCs yielded a PCE of 18.9%. Zhen *et al.*[21] reported two types of dopant-free, donor–acceptor-type polymeric HTMs. In the study, fused-ring indacenodithieno[3,2-*b*]thiophene (IDTT) or indacenodithiophene (IDT) served as the donor, and BDD was employed as the acceptor.

The mentioned polymeric HTMs exhibit tuned energy levels, high hole mobility, good temperature and humidity resistivities, excellent film qualities and a defect passivation ability.[16–22] The corresponding PSCs exhibited an advanced device efficiency and stability.[17,23,24] However, the mentioned efficient polymers structured in a complex way are always synthesized by several tedious steps of the Stille/Suzuki coupling reaction as catalyzed

Tianjin Key Laboratory of Organic Solar Cells and Photochemical Conversion, Tianjin Key Laboratory of Drug Targeting and Bioimaging, School of Chemistry & Chemical Engineering, Tianjin University of Technology, Tianjin 300384, P. R. China. E-mail: zongxueping717@163.com, xuesong@ustc.edu.cn

† Electronic supplementary information (ESI) available. See DOI: 10.1039/d1qm00869b

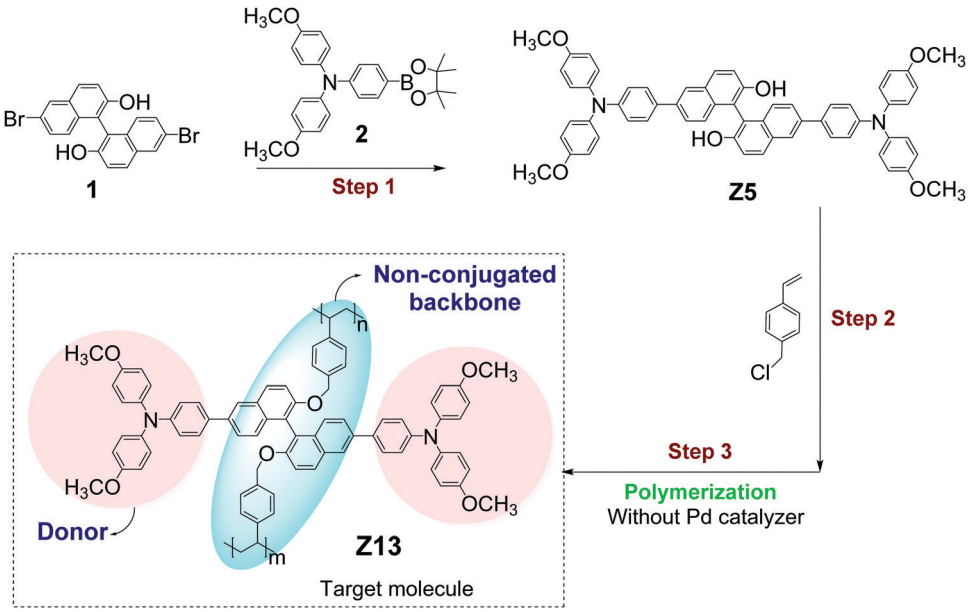

Fig. 1 Synthetic routes for target HTM Z13 and small molecule Z5.

by the noble metal palladium. The molecular weight is difficult to control. In addition, the reaction raw materials, fused rings (*e.g.*, BDD, BDT, IDT and IDTT), are expensive, thereby causing an elevated synthesis cost. Moreover, they are only applied in the n–i–p normal structured PSCs. Polymeric HTMs for p–i–n inverted architecture PSCs (i-PSCs) have been rarely reported. The commercial HTM poly(3,4-ethylenedioxythiophene):poly(styrenesulfonate) (PEDOT:PSS) exhibits a low PCE in i-PSCs due to its inconsistent energy level.[25–28] In 2016, PhNa-1T was incorporated into PEDOT:PSS to build two layers of HTMs, which gave an impressive PCE of 14.7% in i-PSCs.[29] Thus far, only polytriarylamine (PTAA) achieved a significant PCE of 23.37% after a bifunctional molecule was incorporated into inverted i-PSCs.[30] However, the perovskite precursor exhibits poor wettability on the PTAA films, thereby leading to inferior technical reproducibility during the device fabrication.[31] Thus, it is necessary to develop suitable facile effective polymeric HTMs for i-PSCs and to extend their applications in flexible, large-scale and laminated photovoltaic technology.

In this study, a novel polymer was synthesized (Fig. 1), termed as Z13, by using radical polymerization to replace the palladium catalyzed coupling reaction. In such a molecule, the large rigid binaphthalene groups acted as the polymer backbone, while the triphenylamine units were arranged on both sides of the backbone as the donors and side chains. The large π conjugation of naphthalene rings could more effectively provide suitable intermolecular π–π interactions and facilitate the intermolecular charge transport.[22,32] It is noteworthy that the comparatively flexible ether bond (–O–) increased the backbone flexibility and the fractional free volume, thereby contributing to the solubility and film forming properties of the material. Furthermore, the resulting binaphthylether based polymer Z13 was comprehensively investigated for its photophysical parameters, electrochemical properties, photovoltaic performance, *etc.*

Results and discussion

Synthesis and characterization

The synthesis routes are illustrated in Scheme S1 (ESI†), and the detailed synthesis steps are described in the ESI.† Commercially available reagents (*e.g.*, 6,6′-dibromo-1,1′-bi-2-naphthol, 4-methoxy-*N*-(4-methoxyphenyl)-*N*-(4-(4,4,5,5-tetramethyl-1,3,2-dioxaborolan-2-yl)-phenyl)aniline) were adopted to synthesize the polymer through three facile steps *i.e.*, two types of coupling reactions and a radical polymerization reaction. The synthetic cost for Z13 was estimated to be \$45 g^{-1} (Tables S1 and S2, ESI†), a tenth of that of PTAA (\$423 g^{-1}).[33]

Furthermore, the molecular structures of Z13 and Z5 were characterized by FT-IR measurements. According to Fig. 2a, the peak of the hydroxy unit in Z5 was observed at 3452 cm^{-1} for the asymmetric stretching vibration of the O–H group. After the polymerization, this peak disappeared in Z13 spectra. Absorbance at 1329 cm^{-1} detected for Z13 indicated the stretching vibration of the –O– band.[34,35]

The molecular weight distribution was measured with gel permeation chromatography (GPC). The number-average molecular weight (M_n) of Z13 was determined as 6.8 kDa with a polydispersity index (PI) of 1.6. The polymerization reaction conditions were mild. Accordingly, the synthesis process could be reproducible, and the molecular weight could be controllable. Polymer Z13 exhibited a high solubility in common chlorobenzene, toluene and chloroform solvents. As opposed to the abovementioned, Z5 showed a lower solubility in the chlorobenzene solution. Thus, during the PSC fabrication process, Z5 was dissolved in 10–15%(Vol) of *N*,*N*-dimethylformamide and then diluted to 5 mg mL^{-1} with chlorobenzene.

Photophysical and electrochemical properties

The frontier energy levels of hole-transporting materials are essential for charge transfer and capture. According to Fig. 2b

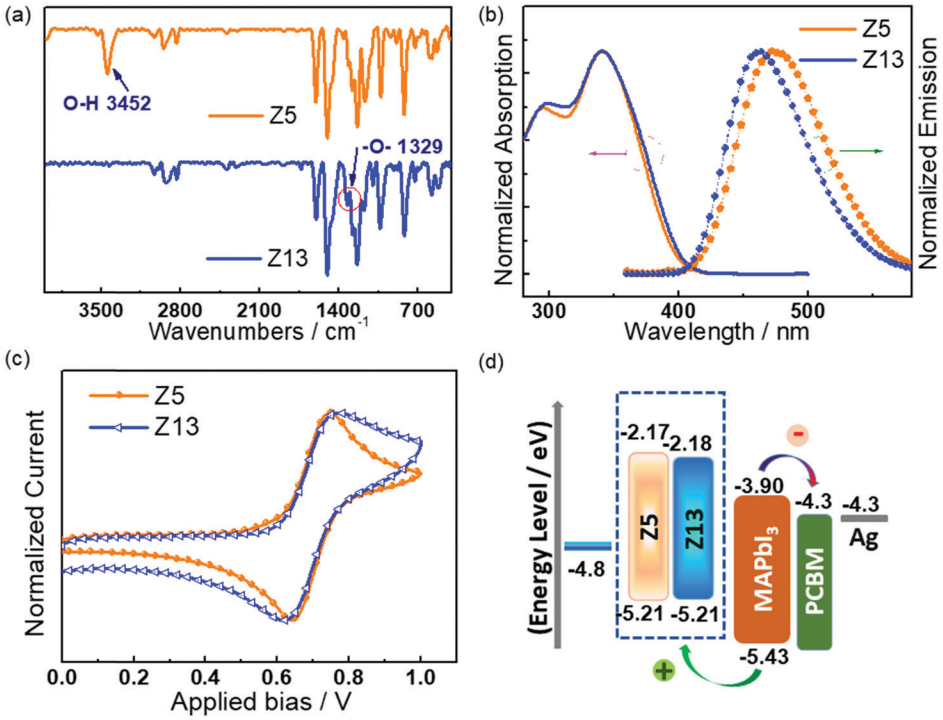

Fig. 2 (a) FT-IR spectra of Z13 and Z5; (b) UV-vis absorption and photoluminescence spectra of HTMs in CH_2Cl_2; (c) cyclic voltammetry curves; and (d) energy levels in i-PSCs.

Table 1 Photophysical, electrochemical and thermal properties exhibited by HTMs

HTMs	λ_{int} [nm]	E_g^{opt} [a] [eV]	E_{HOMO} [b] [V]	HOMO [eV]	LUMO [eV]	T_g [°C]
Z13	409	3.03	0.81	−5.21	−2.18	—
Z5	408	3.04	0.81	−5.21	−2.17	137

[a] $E_g^{opt} = 1240/\lambda_{int}$. λ_{int} represents the intersection point of normalized UV-vis absorption and emission curves.

and Table 1, Z13 and Z5 exhibited similar optical absorption profiles with optical bandgaps (E_g^{opt}) of 3.03 eV and 3.04 eV, respectively. Compared with Z5, the blue shifted fluorescence peak of Z13 might be due to the formation of polymers, which limited the rotation of the monomer, thereby resulting in the increase of the system energy. The highest occupied molecular orbitals (HOMOs) were assessed from the cyclic voltammetry (CV) measurements. As indicated in Fig. 2c, the oxidation–reduction potential (E_{HOMO}) was 0.81 V for Z13 and Z5, and their HOMO was −5.21 eV calculated using the empirical formula $E_{HOMO} = -e(E_{ox} + 4.4)$ (eV).[21,36] E_{HOMO} was standardized with ferrocene (Fig. S1 and Table S3, ESI†). The lowest unoccupied molecular orbital (LUMO) levels were −2.18 eV for Z13 and −2.17 eV for Z5 estimated from the formula E_{LUMO} (eV) = E_{HOMO} (eV) + E_g^{opt}. Both the HOMO and LUMO energy levels of Z13 and Z5 were consistent with those of the perovskite well (Fig. 2d). This enables the simultaneous efficient extraction of holes and prevents the shunt channels from the perovskite to the electron transport layer (PCBM), which could effectively suppress the charge recombination at the HTM/perovskite/ETM interface.

Wettability and thermal properties

In this study, PTAA was used in i-PSCs as a reference HTM to understand the capabilities of newly designed HTMs. For the vital fabrication step in which perovskite is deposited on the upper layer of the HTM films, the wettability of the HTM films significantly affected the growth of perovskite crystals. The contact angles of the perovskite precursor on different HTMs were probed. Fig. 3a illustrates that the 26° of Z5 and 24° of Z13 are smaller than that of PTAA (40°), indicating that the mentioned two HTMs presented good perovskite precursor wettability. In addition, Z5 and Z13 films showed similar hydrophobicity properties to PTAA.

Thermal gravimetric analysis (TGA) and differential scanning calorimetry (DSC) characterization were adopted to illustrate the thermal properties of HTMs. As depicted in Fig. 3b and c, Z5 exhibits a glass transition temperature (T_g) of 137 °C, while Z13 shows no obvious phase transition peak and maintains well an amorphous morphology in the range of −40 to 300 °C. The mentioned result was primarily attributed to the greater steric hindrance and limited rotation around the polymers. In addition, according to Fig. S2 (ESI†), Z13 exhibited an excellent thermal stability with 5% weight loss temperature (T_d, 5%) located at 383 °C and at least 55% residual char yield after 800 °C. Specific to inverted p–i–n type devices, thermal annealing processes were required in the subsequent perovskite growth, the formation of electron-transporting layer and the electrode evaporation. Thus, a good thermal stability and an improved T_g of HTMs could be indispensable to achieve a long-time stability of i-PSCs.[37,38]

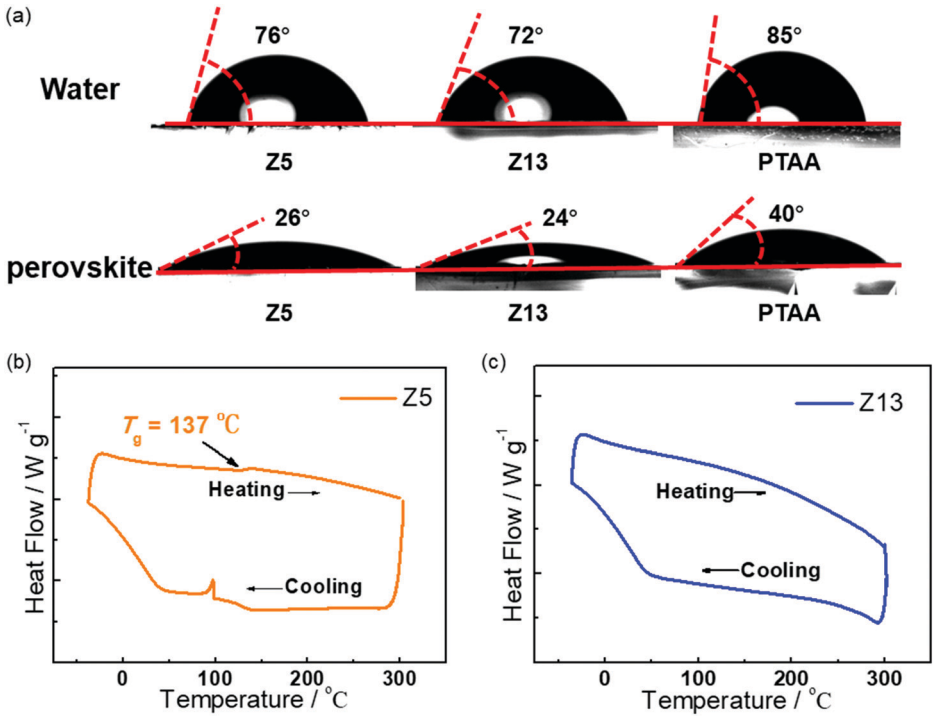

Fig. 3 (a) The contact angles of water and the perovskite precursor on different HTMs. Different scanning calorimetry curves of Z5 (b) and Z13 (c).

Photovoltaic performance of i-PSCs

In i-PSCs, since the surface film morphology of HTMs could impact the growth of upper-layer perovskite crystals, tapping-mode atomic force microscopy (AFM) was probed with glass/ITO/HTM as the substrate. Fig. 4b indicates a smoother and more homogeneous surface with a root-mean-square roughness (R_q) of 2.79 nm for Z13. The R_q values of Z5 and PTAA reached 3.55 nm and 3.18 nm, respectively. Though Z13 achieved a larger M_n compared with Z5, it exhibited a better solubility in the commonly used organic solvents (*e.g.*, chlorobenzene). The smoother HTM surface of Z13 confirmed a better contact within the interface of perovskite and HTLs.

As impacted by the consistent energy levels, enhanced thermal stability and improved surface film morphology, the p–i–n structural i-PSCs were assembled with an architecture of ITO/HTM/$MAPbI_3$/PCBM/BCP/Ag (Fig. 4a). Besides, the commercial HTM, PTAA, was used to fabricate devices for comparison. In order to reduce the partial dissolution of the underlying Z5 layer caused by the perovskite precursor solution, the perovskite layer fabrication process should be operated quickly. Fig. 4c displays the current density–voltage (J–V) plots for the optimized i-PSCs, and the corresponding performance data are summarized in Table 2. The devices based on small molecule Z5 displayed a relatively low PCE of 18.48%, coupled with an open-circuit voltage (V_{oc}) of 1.062 V, a short-circuit current (J_{sc}) of 22.27 mA cm^{-2}, and a fill factor (FF) of 78%. Furthermore, the polymer Z13-based devices exhibited an enlarged V_{oc} of 1.085 V, a J_{sc} of 22.73 mA cm^{-2}, and a FF of 76%, thereby leading to an optimized PCE of 18.80%. Such an efficiency is comparable with that of the i-PSCs using PTAA as the HTM (19.02%).

In addition to the efficiency, a smaller hysteresis was observed for the Z13-fabricated devices between the forward and reverse scans with an absolute hysteresis index of 0.007. As the opposed to that mentioned, the hysteresis index was 0.049 for devices with Z5 and 0.016 for that of PTAA, respectively (Fig. 4e, f, Fig. S3 (ESI†) and Table 2).[28,37] The external quantum efficiency (EQE) spectra were measured to estimate J_{sc} values (Fig. 4d). The integrated J_{sc} values were ordered as Z13 > PTAA > Z5, in good accordance with the results derived from the J–V curves.

J_{sc} differences could be generally associated with charge transfer behavior within the devices.[39] To more specifically confirm the charge transport dynamics between the perovskite and HTL interfaces, the steady-state (PL) and time-resolved photoluminescence (TRPL) were measured. All samples of $MAPbI_3$ with/without HTM films were spin-coated on the ITO surface. As shown in Fig. 5a, an emission peak located at 759 nm was presented for the pristine perovskite film, whereas the PL of perovskite coated on the HTM films was obviously quenched. It is noteworthy that, after Z13 and PTAA were incorporated, the PL intensity was quenched by 76% and 73%, respectively, whereas 60% of PL was quenched by Z5. The stronger PL quenching behaviors of Z13 and PTAA films indicated more efficient hole transfer from the perovskite to HTMs in comparison with Z5.[12,33] TRPL was fitted by a biexponential function $I(t) = A_1 \exp(-t/\tau_1) + A_2 \exp(-t/\tau_2)$ (Fig. 5b), and the corresponding fitted PL lifetime is listed in Table S4 (ESI†). The TRPL decay in perovskite with/without HTMs is primarily dominated by the fast decay process. Notably, τ_1 was shortened to 14.7 ns for $MAPbI_3$-Z13 and 15.8 ns for $MAPbI_3$-PTAA as compared to that for Z5 (16.0 ns).

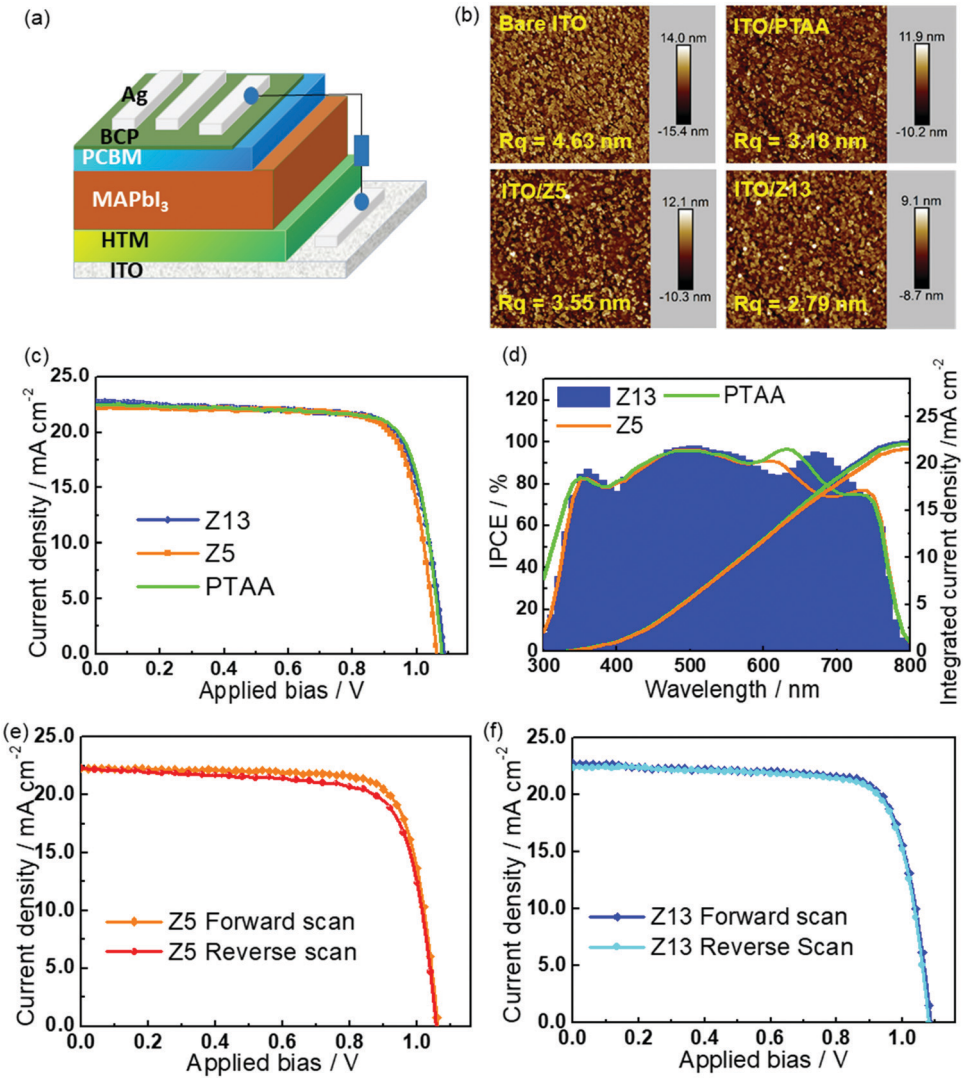

Fig. 4 (a) Device architecture of p–i–n i-PSCs; (b) atomic force microscopy images; (c) J–V curves of the i-PSCs in the forward scanning direction under AM 1.5G, 100 mW cm^{-2} illumination; and (d) EQE spectra of the corresponding i-PSCs; J–V curves measured with forward and reverse scanning for Z5 (e) and Z13 (f), respectively.

Table 2 Photophysical, electrochemical and thermal properties exhibited by HTMs

HTMs	Scan direction	J_{sc} [mA cm^{-2}]	V_{oc} [V]	FF [%]	PCE[a] [%]	Hysteresis[b] index	Average PCE [%]
Z13	Forward	22.73	1.085	76	18.80	—	—
	Reverse	22.37	1.080	77	18.57	0.007	17.85 ± 0.39
Z5	Forward	22.27	1.062	78	18.48	—	—
	Reverse	22.27	1.058	75	17.57	0.049	17.62 ± 0.23
PTAA	Forward	22.48	1.079	78	19.02	—	—
	Reverse	22.32	1.079	78	18.75	0.016	17.43 ± 0.86

[a] Maximal performance. [b] The hysteresis index was calculated by: HI = $[J_{RS}(0.8V_{oc}) - J_{FS}(0.8V_{oc})]/[J_{RS}(0.8V_{oc})]$, here $J_{FS}(0.8V_{oc})$ and $J_{RS}(0.8V_{oc})$ represent the photocurrent density at 80% of V_{oc} with the forward scan (FS) and reverse scan (FS), respectively.

The mentioned results were in good accordance with the steady-state PL spectra.[40] As collected in Fig. 7, the fresh perovskite crystal (PVSK, 0 h) coated on Z13 and PTAA films was larger and sharper in contrast to that of Z5. Furthermore, Z13 afforded a more uniform perovskite morphology. A poor crystallinity morphology of $MAPbI_3$ resulted in a lower J_{sc}, consequently, Z5-based i-PSCs presented a lower efficiency.

Besides the J_{sc} distinction, as illustrated in Fig. 4c and Table 2, we found a low V_{oc} value for Z5-based i-PSCs. Specifically, there are two factors affecting the V_{oc} level: the energy level alignment and charge recombination behaviors.[12,30,41,42] For the similar energy levels between Z13 and Z5, carrier recombination was considered to be a major influence for V_{oc} loss. The electrochemical impedance spectroscopy (EIS) characterization was conducted to probe the internal electrical characteristics in the dark ranging from 1 MHz to 20 Hz. The obtained data were fitted by an equivalent circuit model displayed in Fig. S4 (ESI†). The series resistance (R_s) at low frequency relates to the properties of electron-transport materials (ETMs). Recombination resistance (R_{rec}) could represent the

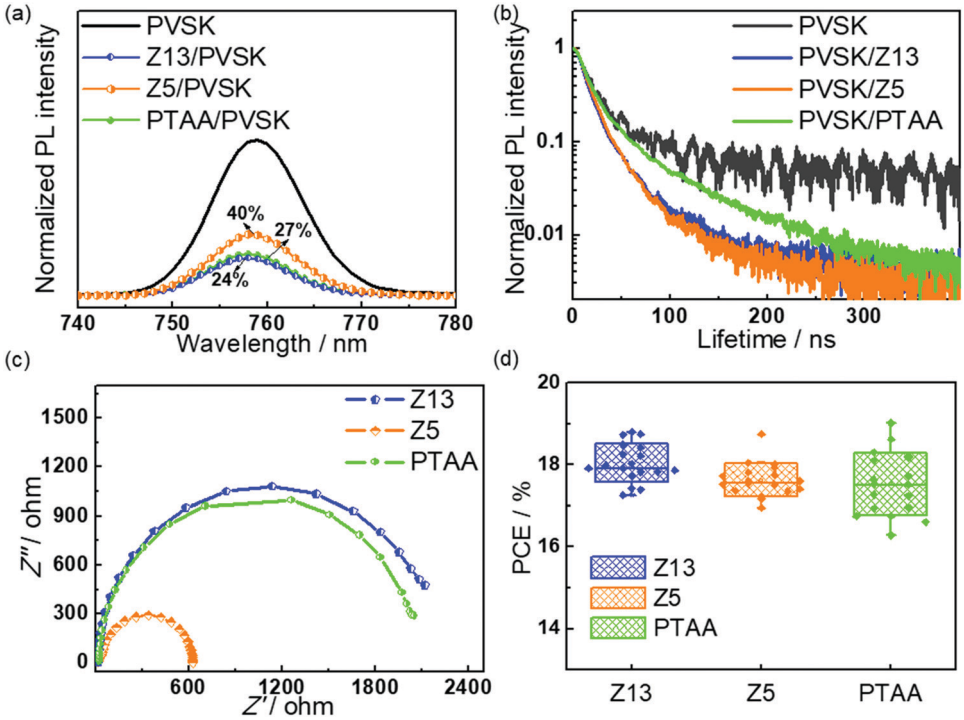

Fig. 5 (a) Steady-state photoluminescence; (b) time-resolved photoluminescence; (c) electrochemical impedance spectroscopy characterization; and (d) PCE variations for 18 individual i-PSCs with different HTMs.

charge recombination resistance at low frequency. R_{rec} of i-PSCs reached 1.2 KΩ for Z13, 1.1 KΩ for PTAA and 0.4 KΩ for Z5, respectively. A higher R_{rec} could indicate a lower recombination rate, so the device with PTAA and Z13 exhibited a higher V_{oc} as impacted by the suppressed charge recombination.[31,43]

To further verify whether the Z13-based i-PSCs outperformed commercial PTAA, *J–V* results obtained from 15 individual i-PSCs are plotted in Fig. 5d and summarized in Tables S5–S7 (ESI†). As demonstrated in the histogram of PCE, Z13/Z5-based displayed an improved average PCE of 17.86% and 17.62%, respectively. Furthermore, Z13/Z5-based displayed a higher reproducibility with a narrower efficiency distribution in contrast to PTAA.

Device stability

Thermal tolerance for the perovskite coated upper layer of HTMs could be a crucial factor to evaluate the potential application in extreme environments. To assess the thermal device stability, all unencapsulated i-PSCs with different HTMs were kept under a N_2 atmosphere (30% relative humidity) at 85 °C. The i-PSCs endowed with Z13 maintained over 86% of the initial performance after 45 h aging at 85 °C, whereas the references with PTAA and Z5 suffered an obvious decreased performance. In particular, the PTAA-based device retained only 60% of the original PCE after 45 h. Fig. 6c provides a clear evolution of perovskite film-degradation. In comparison to the fresh one, the perovskite film with PTAA decomposed to a pale-yellow film and that with Z5 displayed a slightly yellow surface, whereas the perovskite film coated on Z13 retained a dark uniform appearance after heating for 45 h.

The mentioned degradation of the perovskite morphology was further illustrated by X-ray diffraction (XRD) and scanning electron microscopy (SEM). As marked in the XRD spectra (Fig. 6b), peak 1* belonged to the decomposed PbI_2, while peak 2* was ascribed to the main characteristic peak for the (110) plane of the perovskite.[44] In all fresh perovskite films, no PbI_2 impurity signal was observed. Moreover, all the bare perovskite crystals were sharp (Fig. 7). After 24 h, a PbI_2 impurity signal was detected for the mentioned three HTMs. The peak intensity ratio between PbI_2 and the (110) plane of the perovskite is ordered in the sequence of Z13, Z5 and PTAA. Thus, perovskite coated on Z13 was less degraded, so the perovskite morphology remained sharp. When heated for 45 h, the thermal-stability difference in perovskite films became more pronounced. The small crystal in the Z5-based perovskite was decomposed, and a significant fraction of the perovskite crystals for PTAA was decomposed. As opposed to that mentioned, the Z13-based perovskite crystal retained uniform and dense morphology. The XRD and SEM results were in good agreement with the PCE evolution. For this reason, a better perovskite crystal quality was achieved on the surface of Z13 films and further an optimized device thermal-stability was obtained as opposed to that of the small molecule (Z5) and commercial PTAA. Given the limitations of complex synthetic routes for PTAA and inferior thermal stability of the corresponding i-PSCs, Z13 validates more promising applications in laminated silicon-perovskite and the roll-to-roll process for large-scale devices.

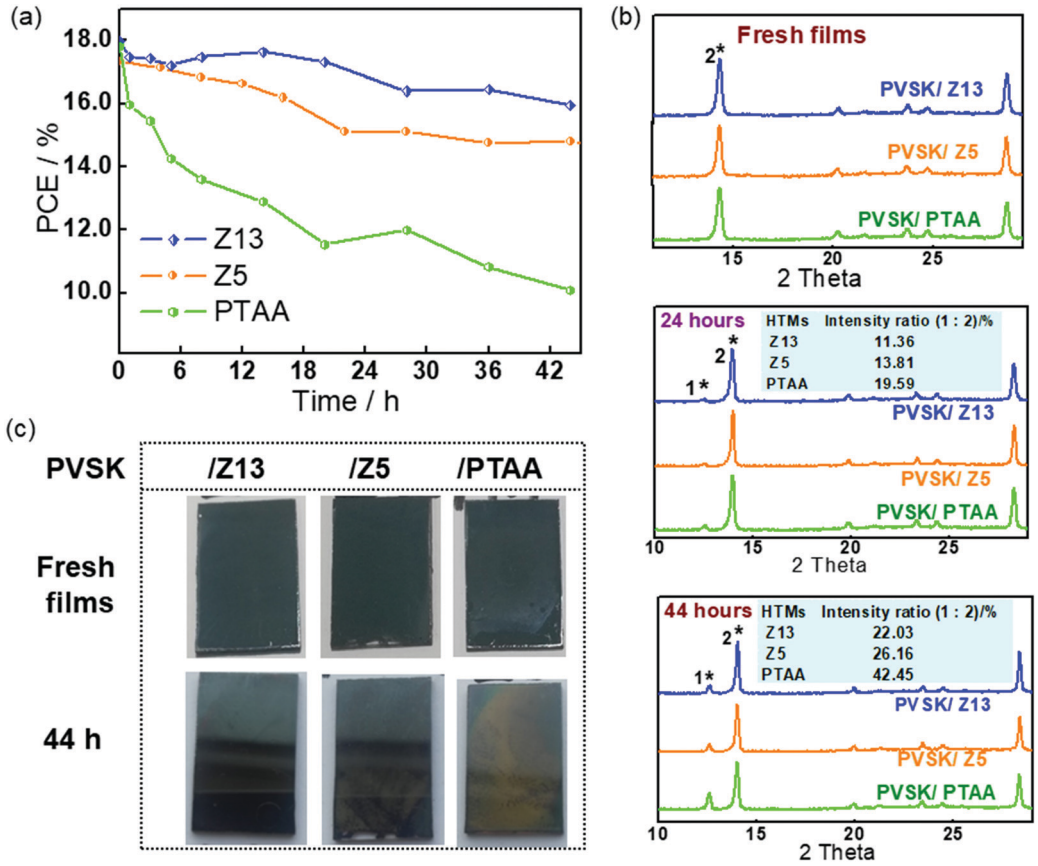

Fig. 6 Stability analysis. (a) PCE evolution of unencapsulated i-PSCs heated at 85 °C under a N_2 atmosphere (30% relative humidity); (b) XRD pattern evolution of i-PSCs with different HTMs; and (c) perovskite (PVSK) film-degradation evolution during heating.

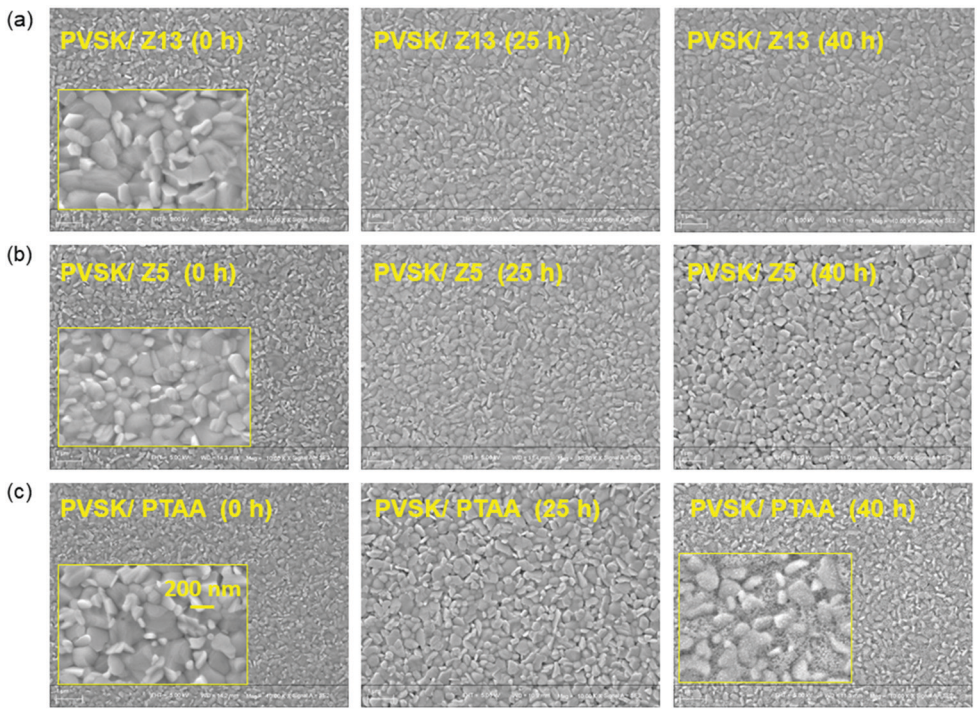

Fig. 7 The morphology degradation of perovskite films deposited on the different HTM layers (a) Z13; (b) Z5; and (c) PTAA.

Conclusions

In this work, a facile and rational design of a novel polymer was presented, termed as Z13. The polymerization reaction conditions were mild and reproducible, and the molecular weight was controllable. The comparative flexible ether bond (–O–) in the Z13 structure optimized the backbone flexibility and fractional free volume, and it further improved the solubility and film forming properties. The resulting binaphthyl-ether based polymer Z13 facilitated the thermal-stability and the charge transfer as compared with those of the small molecule (termed Z5) and commercial PTAA. When employed in p–i–n structured perovskite solar cells, the devices with Z13 exhibited a power conversion efficiency of 18.80%, which was comparable with that of PTAA (19.02%). In addition, the Z13-fabricated devices were observed to exhibit smaller hysteresis. Furthermore, a better perovskite crystal quality was obtained on the surface of Z13 films, thereby ensuring an improved device thermal-stability in comparison to references PTAA and Z5. This study proposed a guideline to access polymeric HTMs achieving high efficiency and good thermal stability.

Experimental

Synthetic procedures of compounds Z5 and Z13 are listed in Fig. 1. The chemical structure of novel HTMs was determined by ^{1}H NMR. All the materials and solvents were purchased without further purification. Some characterization studies of HTMs and i-PSCs are presented in the ESI.†

Conflicts of interest

There are no conflicts to declare.

Acknowledgements

This work was supported by the National Natural Science Foundation of China (22005218, 22078248 and 22075210). The authors would like to thank Hui Wang for the help in FESEM testing and Gang-ri Cai for the help in AFM imaging.

Notes and references

1 A. Kojima, K. Teshima, Y. Shirai and T. Miyasaka, Organometal halide perovskites as visible-light sensitizers for photovoltaic cells, *J. Am. Chem. Soc.*, 2009, **131**, 6050–6051.
2 National Renewable Energy Laboratory, https://www.nrel.gov/pv/cell-efficiency.html.
3 M. Kim, G.-H. Kim, T. K. Lee, I. W. Choi, H. W. Choi, Y. Jo, Y. J. Yoon, J. W. Kim, J. Lee, D. Huh, H. Lee, S. K. Kwak, J. Y. Kim and D. S. Kim, Methylammonium chloride induces intermediate phase stabilization for efficient perovskite solar cells, *Joule*, 2019, **3**, 2179–2192.
4 E. H. Jung, N. J. Jeon, E. Y. Park, C. S. Moon, T. J. Shin, T.-Y. Yang, J. H. Noh and J. Seo, Efficient, stable and scalable perovskite solar cells using poly(3-hexylthiophene), *Nature*, 2019, **567**, 511–515.
5 R. Lin, K. Xiao, Z. Qin, Q. Han, C. Zhang, M. Wei, M. I. Saidaminov, Y. Gao, J. Xu, M. Xiao, A. Li, J. Zhu, E. H. Sargent and H. Tan, Monolithic all-perovskite tandem solar cells with 24.8% efficiency exploiting comproportionation to suppress Sn(II) oxidation in precursor ink, *Nat. Energy*, 2019, **4**, 864–873.
6 A. Al-Ashouri, E. Köhnen, B. Li, A. Magomedov, H. Hempel, P. Caprioglio, J. A. Márquez, A. B. Morales Vilches, E. Kasparavicius, J. A. Smith, N. Phung, D. Menzel, M. Grischek, L. Kegelmann, D. Skroblin, C. Gollwitzer, T. Malinauskas, M. Jošt, G. Matič, B. Rech, R. Schlatmann, M. Topič, L. Korte, A. Abate, B. Stannowski, D. Neher, M. Stolterfoht, T. Unold, V. Getautis and S. Albrecht, Monolithic perovskite/silicon tandem solar cell with >29% efficiency by enhanced hole extraction, *Science*, 2020, **370**, 1300.
7 Y. Cai, J. Wen, Z. Liu, F. Qian, C. Duan, K. He, W. Zhao, S. Zhan, S. Yang, J. Cui and S. Liu, Graded 2D/3D (CF3-PEA)-2FA0.85MA0.15Pb2I7/FA0.85MA0.15PbI3 heterojunction for stable perovskite solar cell with an efficiency over 23.0%, *J. Energy Chem.*, 2022, **65**, 480–489.
8 H. Zhang, B. Wu, Q. Wu, Z. Wang, S. Xue and M. Liang, Arm modulation of triarylamines to fine-tune the properties of linear D–π–D HTMs for robust higher performance perovskite solar cells, *Mater. Chem. Front.*, 2021, **5**, 4604–4614.
9 M. Li, J. Wu, G. Wang, B. Wu, Z. Sun, S. Xue, Q. Qiao and M. Liang, The donor-dependent methoxy effects on the performance of hole-transporting materials for perovskite solar cells, *J. Energy Chem.*, 2020, **47**, 10–17.
10 Y. Cheng, Q. Fu, X. Zong, Y. Dong, W. Zhang, Q. Wu, M. Liang, Z. Sun, Y. Liu and S. Xue, Coplanar phenanthro[9,10-*D*]imidazole based hole-transporting material enabling over 19%/21% efficiency in inverted/regular perovskite solar cells, *Chem. Eng. J.*, 2021, **421**, 129823.
11 Q. Fu, Z. Xu, X. Tang, T. Liu, X. Dong, X. Zhang, N. Zheng, Z. Xie and Y. Liu, Multifunctional two-dimensional conjugated materials for dopant-free perovskite solar cells with efficiency exceeding 22%, *ACS Energy Lett.*, 2021, 1521–1532.
12 S. Öz, A. K. Jena, A. Kulkarni, K. Mouri, T. Yokoyama, I. Takei, F. Ünlü, S. Mathur and T. Miyasaka, Lead(II) propionate additive and a dopant-free polymer hole transport material for CsPbI2Br perovskite solar cells, *ACS Energy Lett.*, 2020, **5**, 1292–1299.
13 Y. Chen, X. Xu, N. Cai, S. Qian, R. Luo, Y. Huo and S. W. Tsang, Rational design of dopant-free coplanar D–π–D hole-transporting materials for high-performance perovskite solar cells with fill factor exceeding 80%, *Adv. Energy Mater.*, 2019, **9**, 1901268.
14 J. Wu, C. Liu, B. Li, F. Gu, L. Zhang, M. Hu, X. Deng, Y. Qiao, Y. Mao, W. Tan, Y. Tian and B. Xu, Side-chain polymers as dopant-free hole-transporting materials for perovskite solar cells—the impact of substituents' positions in carbazole on device performance, *ACS Appl. Mater. Interfaces*, 2019, **11**, 26928–26937.
15 W. Chen, T. Liu, X. Sun, F. Guo, Y. Wang, C. Shi, R. Ghadari and F. Kong, Facile synthesis of simple arylamine-substituted naphthalene derivatives as hole-transporting materials for

efficient and stable perovskite solar cells, *J. Power Sources*, 2019, **425**, 87–93.

16 G.-W. Kim, J. Lee, G. Kang, T. Kim and T. Park, Donor–acceptor type dopant-free, polymeric hole transport material for planar perovskite solar cells (19.8%), *Adv. Energy Mater.*, 2018, **8**, 1701935.

17 L. Zhang, C. Liu, X. Wang, Y. Tian, A. K. Y. Jen and B. Xu, Side-chain engineering on dopant-free hole-transporting polymers toward highly efficient perovskite solar cells (20.19%), *Adv. Funct. Mater.*, 2019, **29**, 1904856.

18 F. Qi, X. Deng, X. Wu, L. Huo, Y. Xiao, X. Lu, Z. Zhu and A. K. Y. Jen, A dopant-free polymeric hole-transporting material enabled high fill factor over 81% for highly efficient perovskite solar cells, *Adv. Energy Mater.*, 2019, **9**, 1902600.

19 F. Zhang, Z. Yao, Y. Guo, Y. Li, J. Bergstrand, C. J. Brett, B. Cai, A. Hajian, Y. Guo, X. Yang, J. M. Gardner, J. Widengren, S. V. Roth, L. Kloo and L. Sun, Polymeric, cost-effective, dopant-free hole transport materials for efficient and stable perovskite solar cells, *J. Am. Chem. Soc.*, 2019, **141**, 19700–19707.

20 X. Jiang, X. Liu, J. Zhang, S. Ahmad, D. Tu, W. Qin, T. Jiu, S. Pang, X. Guo and C. Li, Simultaneous hole transport and defect passivation enabled by a dopant-free single polymer for efficient and stable perovskite solar cells, *J. Mater. Chem. A*, 2020, **8**, 21036–21043.

21 G. You, Q. Zhuang, L. Wang, X. Lin, D. Zou, Z. Lin, H. Zhen, W. Zhuang and Q. Ling, Dopant-free, donor–acceptor-type polymeric hole-transporting materials for the perovskite solar cells with power conversion efficiencies over 20%, *Adv. Energy Mater.*, 2019, **10**, 1903146.

22 K. K. Sonigara, Z. Shao, J. Prasad, H. K. Machhi, G. Cui, S. Pang and S. S. Soni, Organic ionic plastic crystals as hole transporting layer for stable and efficient perovskite solar cells, *Adv. Funct. Mater.*, 2020, **30**, 2001460.

23 G. W. Kim, H. Choi, M. Kim, J. Lee, S. Y. Son and T. Park, Hole transport materials in conventional structural (n–i–p) perovskite solar cells: From past to the future, *Adv. Energy Mater.*, 2020, **10**, 1903403.

24 Z. Yao, F. Zhang, Y. Guo, H. Wu, L. He, Z. Liu, B. Cai, Y. Guo, C. J. Brett, Y. Li, C. V. Srambickal, X. Yang, G. Chen, J. Widengren, D. Liu, J. M. Gardner, L. Kloo and L. Sun, Conformational and compositional tuning of phenanthrocarbazole-based dopant-free hole-transport polymers boosting the performance of perovskite solar cells, *J. Am. Chem. Soc.*, 2020, **142**, 17681–17692.

25 N. Liu, X. Zong, Z. Wang, T. Cui, M. Liang, Y. Zhang and S. Xue, LiTFSI/TBP-free hole transport materials with non-linear Π-conjugation for efficient inverted perovskite solar cells, *Electrochim. Acta*, 2019, **296**, 283–293.

26 Y. Lu, X. Zong, Y. Wang, W. Zhang, Q. Wu, M. Liang and S. Xue, Noncovalent functionalization of hole-transport materials with multi-walled carbon nanotubes for stable inverted perovskite solar cells, *J. Mater. Chem. C*, 2019, **7**, 14306–14313.

27 J. Zhang, Q. Sun, Q. Chen, Y. Wang, Y. Zhou, B. Song, X. Jia, Y. Zhu, S. Zhang, N. Yuan, J. Ding and Y. Li, Dibenzo[*b*,*d*]thiophene-cored hole-transport material with passivation effect enabling the high-efficiency planar p–i–n perovskite solar cells with 83% fill factor, *Sol. RRL*, 2019, **4**, 1900421.

28 X. Lin, D. Cui, X. Luo, C. Zhang, Q. Han, Y. Wang and L. Han, Efficiency progress of inverted perovskite solar cells, *Energy Environ. Sci.*, 2020, **13**, 3823–3847.

29 J. W. Jo, M.-S. Seo, M. Park, J.-Y. Kim, J. S. Park, I. K. Han, H. Ahn, J. W. Jung, B.-H. Sohn, M. J. Ko and H. J. Son, Improving performance and stability of flexible planar-heterojunction perovskite solar cells using polymeric hole-transport material, *Adv. Funct. Mater.*, 2016, **26**, 4464–4471.

30 F. Li, X. Deng, F. Qi, Z. Li, D. Liu, D. Shen, M. Qin, S. Wu, F. Lin, S.-H. Jang, J. Zhang, X. Lu, D. Lei, C.-S. Lee, Z. Zhu and A. K. Y. Jen, Regulating surface termination for efficient inverted perovskite solar cells with greater than 23% efficiency, *J. Am. Chem. Soc.*, 2020, **142**, 20134–20142.

31 H. Ma, L. Yuan, Q. Chen, J. Fu, J. Zhang, Z. Jiang, B. Dong, Y. Zhou, S. Yin and B. Song, Conjugated copolymers as doping- and annealing-free hole transport materials for highly stable and efficient p–i–n perovskite solar cells, *J. Mater. Chem. A*, 2021, **9**, 2269–2275.

32 H. Guo, H. Zhang, C. Shen, D. Zhang, S. Liu, Y. Wu and W. H. Zhu, A coplanar pi-extended quinoxaline based hole-transporting material enabling over 21% efficiency for dopant-free perovskite solar cells, *Angew. Chem., Int. Ed.*, 2021, **60**, 2674–2679.

33 Y. Wang, Q. Liao, J. Chen, W. Huang, X. Zhuang, Y. Tang, B. Li, X. Yao, X. Feng, X. Zhang, M. Su, Z. He, T. J. Marks, A. Facchetti and X. Guo, Teaching an old anchoring group new tricks: Enabling low-cost, eco-friendly hole-transporting materials for efficient and stable perovskite solar cells, *J. Am. Chem. Soc.*, 2020, **142**, 16632–16643.

34 G. Deng, J. Luo, S. Liu, Y. Wang, X. Zong and S. Xue, Molecular design and characterization of new polyimides based on binaphthyl-ether diamines for gas separation, *Sep. Purif. Technol.*, 2020, **235**, 116218.

35 G. Deng, J. Luo, X. Liu, S. Liu, Y. Wang, X. Zong and S. Xue, Fabrication of high-performance mixed-matrix membranes *via* constructing an *in situ* crosslinked polymer matrix for gas separations, *Sep. Purif. Technol.*, 2021, **271**, 118859.

36 J. Wang, H. Zhang, B. Wu, Z. Wang, Z. Sun, S. Xue, Y. Wu, A. Hagfeldt and M. Liang, Indeno[1,2-*b*]carbazole as methoxy-free donor group: Constructing efficient and stable hole-transporting materials for perovskite solar cells, *Angew. Chem., Int. Ed.*, 2019, **58**, 15721–15725.

37 B. Li, K. Yang, Q. Liao, Y. Wang, M. Su, Y. Li, Y. Shi, X. Feng, J. Huang, H. Sun and X. Guo, Imide-functionalized triarylamine-based donor–acceptor polymers as hole transporting layers for high-performance inverted perovskite solar cells, *Adv. Funct. Mater.*, 2021, **31**, 2100332.

38 Y. Wang, W. Chen, L. Wang, B. Tu, T. Chen, B. Liu, K. Yang, C. W. Koh, X. Zhang, H. Sun, G. Chen, X. Feng, H. Y. Woo, A. B. Djurisic, Z. He and X. Guo, Dopant-free small-molecule hole-transporting material for inverted perovskite solar cells with efficiency exceeding 21, *Adv. Mater.*, 2019, **31**, 1902781.

39 E. Akman and S. Akin, Poly(*N*,*N*′-bis-4-butylphenyl-*N*,*N*′-bisphenyl)benzidine-based interfacial passivation strategy

promoting efficiency and operational stability of perovskite solar cells in regular architecture, *Adv. Mater.*, 2021, **33**, 2006087.

40 Q. Han, Y. Bai, J. Liu, K.-z. Du, T. Li, D. Ji, Y. Zhou, C. Cao, D. Shin, J. Ding, A. D. Franklin, J. T. Glass, J. Hu, M. J. Therien, J. Liu and D. B. Mitzi, Additive engineering for high-performance room-temperature-processed perovskite absorbers with micron-size grains and microsecond-range carrier lifetimes, *Energy Environ. Sci.*, 2017, **10**, 2365–2371.

41 W. Xu, F. He, M. Zhang, P. Nie, S. Zhang, C. Zhao, R. Luo, J. Li, X. Zhang, S. Zhao, W.-D. Li, F. Kang, C.-W. Nan and G. Wei, Minimizing voltage loss in efficient all-inorganic CsPbI2Br perovskite solar cells through energy level alignment, *ACS Energy Lett.*, 2019, **4**, 2491–2499.

42 J. Ma, J. Su, Z. Lin, L. Zhou, J. He, J. Zhang, S. Liu, J. Chang and Y. Hao, Improve the oxide/perovskite heterojunction contact for low temperature high efficiency and stable all-inorganic CsPbI2Br perovskite solar cells, *Nano Energy*, 2020, **67**, 104241.

43 T. Zheng, B. Fan, Y. Zhao, B. Jin, L. Fan and R. Peng, Tailored conductive fullerenes-based passivator for efficient and stable inverted perovskite solar cells, *J. Colloid Interface Sci.*, 2021, **598**, 229–237.

44 Y. Hu, Y. Shan, Z. Yu, H. Sui, T. Qiu, S. Zhang, W. Ruan, Q. Xu, M. Jiao, D. Wang, Y. Wu, C. Yang and F. Xu, Incorporation of γ-aminobutyric acid and cesium cations to formamidinium lead halide perovskites for highly efficient solar cells, *J. Energy Chem.*, 2022, **64**, 561–567.

